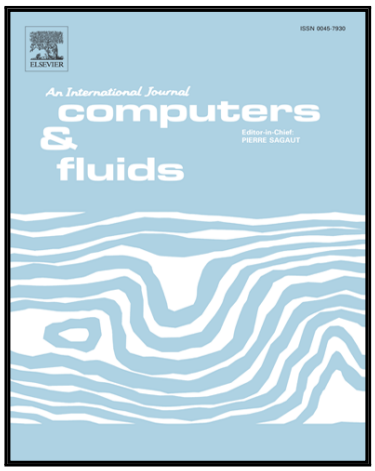

An efficient Discrete Element Lattice Boltzmann model for simulation of particle-fluid, particle-particle interactions

Pei Zhang, S.A. Galindo-Torres, Hongwu Tang, Guangqiu Jin, A. Scheuermann, Ling Li

PII: S0045-7930(17)30032-4
DOI: 10.1016/j.compfluid.2017.01.019
Reference: CAF 3385

To appear in: *Computers and Fluids*

Received date: 18 November 2016
Revised date: 6 January 2017
Accepted date: 23 January 2017

Please cite this article as: Pei Zhang, S.A. Galindo-Torres, Hongwu Tang, Guangqiu Jin, A. Scheuermann, Ling Li, An efficient Discrete Element Lattice Boltzmann model for simulation of particle-fluid, particle-particle interactions, *Computers and Fluids* (2017), doi: 10.1016/j.compfluid.2017.01.019

An efficient Discrete Element Lattice Boltzmann model for simulation of particle-fluid, particle-particle interactions

Pei Zhang[a], S.A. Galindo-Torres[b,c], Hongwu Tang[a,*], Guangqiu Jin[a], A. Scheuermann[b], Ling Li[b]

[a]*State Key Laboratory of Hydrology-Water Resources and Hydraulic Engineering, Hohai University, Nanjing, China*
[b]*School of Civil Engineering, University of Queensland, Queensland, Australia*
[c]*School of Mathematics and Physics, University of Queensland, Queensland, Australia*

Abstract

In this study, an efficient Discrete Element Lattice Boltzmann Model (DE-LBM) is introduced to simulate mechanical behaviours of multiphase systems involving particle-fluid and particle-particle interactions. The LBM is based on the Multiple Relaxation Time (MRT-LBM) formalism for the fluid phase and the Discrete Element Method for particle motions. A novel algorithm is developed for detecting the particle contact base on particle overlapping areas computed directly from the grid-based LBM data. This contact algorithm achieves the same accuracy in determining the particle contact as provided by the Hertz contact model but is far more efficient computationally. The DE-LBM coupling approach is also modified to unify the different schemes developed previously. A modified Verlet List method for updating the solid occupation fraction is proposed to further speed up the simulation. The new model is validated by a series of simulations including the single particle settling and well-known 'Drafting, Kissing and Tumbling' (DKT) phenomenon found in suspensions. The settling of a large number (2500) of particles in a still fluid is also simulated with predicted concentration profiles matching well the analytic solution. These applications demonstrate the potential of the present DE-LBM model as a powerful numerical tool for simulating multiphase particulate systems encountered in many engineering and science

*Corresponding author
Email address: hwtang@hhu.edu.cn (Hongwu Tang)

disciplines.

1. Introduction

Particles moving in flows are frequently encountered in both natural and industrial fields. Examples can be found from sediment transport in oceans and rivers, red cells moving within the blood plasma to particle mixing in a fluidized-bed reactor used widely in the chemical industry. Particle-fluid and particle-particle interactions play an important role in these processes, and underlie complex system behaviours at different scales.

The problem has attracted interests of many researchers and been studied experimentally [1–16] However, experiments cannot always provide enough information, particularly about the mechanics occurring at the particle scale, due to measurement limitations. An alternative approach is through numerical modelling by means of particle-based simulation methods. As computational resources continue to improve, particle-based methods show great abilities in replicating details of fluid flows and particle motions at both the microscopic and macroscopic scales. In solid mechanics, the Discrete Element Method [17] (DEM) has been successfully applied to predict the behaviours of granular materials and dry soils [18, 19]. Coupling DEM with the Lattice Boltzmann Method (LBM) has been carried out to enable simulations of fluid-particle interactions [20]. Ladd [21] modified the original LBM for spheres settling in a viscous fluid with a lubrication model to avoid collisions between solid particles [22]. Cate et al. [12] reported a good agreement between simulation results given by Ladd's method and experimental data under conditions of relatively low Reynolds numbers with the wall boundary effect also considered. Cook et al. [23] presented a coupled Discrete Element-Lattice Boltzmann method where particle collisions are solved by a contact model. This DE-LBM method was also coupled with the Smagorinsky subgrid turbulence module to overcome the low Reynolds number limitation [24]. Spherical particles were employed in these studies. Galindo-Torres [20, 25] extended the DE-LBM model for general shaped particles (even non-convex ones) by using the sphero-polyhedron technique [26–29]. Furthermore, multiphase and multicomponent fluids with particle motions were also considered [20]. Indeed the DE-LBM has been already applied to many areas: for example, Zhang et al. [30] studied the settling dynamics of irregularly shaped particles over a wide range of Reynolds numbers; Wang et al. [31, 32] presented simulations for the gas-solid fluidization; and soil behaviours due to

locally injected fluid were modelled by Cui et al. [33]. However a key obstacle for applying the DE-LBM to a large scale problem is the computation cost within the limit of available computer resources since both DEM and LBM are computationally intensive.

The main goal of this study is to develop an efficient DE-LBM where the particle-particle contact detection and the particle-grid immersion problems are combined into one, saving greatly the computational time. The solution uses the information of the overlapping area between the DE particles and the LBM grid cells to construct the contact area between DE particles and deduce the contact force. Optimization techniques are also discussed to further enhance the method.

The following of the paper is organized as follows: Sec. 2 describes the LBM and DEM. The modified coupling approach is then presented with a novel contact detection algorithm and contact model. Sec. 3 shows a series of numerical examples to validate the new DE-LBM model. An application of this model to the settling of large numbers of particles is elaborated in Sec. 4. Finally Sec. 5 presents conclusions from the present work.

2. Methodology

2.1. Lattice Boltzmann method for fluid

The Lattice Boltzmann Equation (LBE) is employed to solve the fluid flow problem [34, 35] using the D2Q9 model with the space divided into four-square lattices. The velocity domain is discretized into 9 velocity vectors as shown in Fig. 1. The discrete velocity vectors are defined as follows:

$$\overrightarrow{e}_i = \begin{cases} 0, & i = 0, \\ (\pm 1, 0,), (0, \pm 1), & i = 1 \text{ to } 4, \\ (\pm 1, \pm 1), & i = 5 \text{ to } 8, \end{cases}$$

Based on the Chapman-Enskog expansion of the Boltzmann equation, an evolution rule is applied to every distribution function [36]:

$$f_i(\overrightarrow{x} + \overrightarrow{e}_i \delta t, t + \delta t) = f_i(\overrightarrow{x}, t) + \Omega_{col}, \tag{1}$$

where f_i is the probability distribution function, $\overrightarrow{x}$ is the position of the local lattice, δt is the time step and Ω_{col} is the collision operator. The most widely

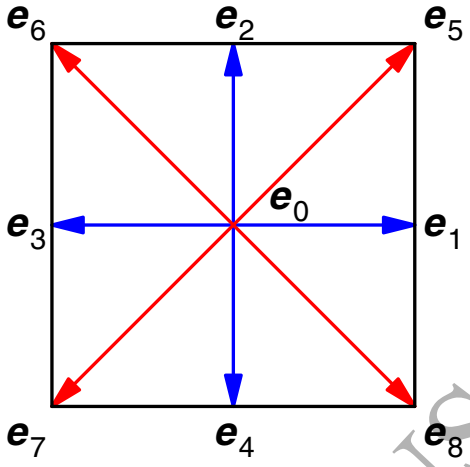

Figure 1: D2Q9 model.

used form of Ω_{col} is the so-called Bhatnagar-Gross-Krook (BGK) collision operator: $\Omega_{col} = \frac{\delta t}{\tau}(f_i^{eq} - f_i)$, with f_i^{eq} the equilibrium distribution given by,

$$f_i^{eq} = \omega_i \rho \left(1 + 3\frac{\overrightarrow{e}_i \cdot \overrightarrow{u}}{C^2} + \frac{9(\overrightarrow{e}_i \cdot \overrightarrow{u})^2}{2C^4} - \frac{3u^2}{2C^2}\right), \tag{2}$$

where $C = \delta x/\delta t$ is the characteristic lattice velocity (δx is the lattice size). The weights are $\omega_0 = 4/9$, $\omega_i = 1/9$ for i =1 to 4, and $\omega_i = 1/36$ for i =5 to 8.

The BGK collision operator assumes that the collision only depends on a dimensionless relaxation time τ. However, It's found that the simulations become unstable when the value of τ is close to 0.5 [20]. Therefore, the BGK collision operator is only suitable for flow at relatively low Reynolds numbers. To overcome this limitation, the multiple relaxation time (MRT) collision operator is adopted in this study as follows:

$$\Omega_{col} = \hat{\mathbf{M}}^{-1}\hat{\mathbf{S}}(m_i^{eq} - m_i), \tag{3}$$

with $m_i = \hat{\mathbf{M}} f_i$, where $\hat{\mathbf{M}}$ is a matrix used to transform the probability distribution function f_i to velocity moments linearly. For the D2Q9 model, the moments are arranged as: $m_0 = \rho$; $m_1 = e$; $m_2 = \epsilon$; $m_{3,5} = j_{x,y}$ are components of the momentum $\overrightarrow{j} = (j_x, j_y) = \rho\overrightarrow{u}$; $m_{4,6} = q_{x,y}$ are related to components of the heat flux $\overrightarrow{q} = (q_x, q_y)$; $m_7 = p_{xx}$; and $m_8 = p_{xy}$ are related

to the components of the strain-rate tensor. The equilibrium moments are the functions of conserved moments (density ρ and moment density $\overrightarrow{j}$) and the non-conserved moments are given by [37],

$$\begin{aligned} m_1^{eq} = e^{eq} = \rho(-2 + 3\overrightarrow{j}\cdot\overrightarrow{j}), \quad m_2^{eq} = \epsilon^{eq} = \rho(1 - 3\overrightarrow{j}\cdot\overrightarrow{j}), \\ m_4^{eq} = q_x^{eq} = -j_x, \qquad\qquad m_6^{eq} = q_y^{eq} = -j_y, \\ m_7^{eq} = p_{xx}^{eq} = \tfrac{{j_x}^2 - {j_y}^2}{\rho}, \qquad\qquad m_8^{eq} = p_{xy}^{eq} = \tfrac{j_x j_y}{\rho}, \end{aligned} \tag{4}$$

the transformation matrix is defined as:

$$\hat{\mathbf{M}} = \begin{bmatrix} 1 & 1 & 1 & 1 & 1 & 1 & 1 & 1 & 1 \\ -4 & -1 & -1 & -1 & -1 & 2 & 2 & 2 & 2 \\ 4 & -2 & -2 & -2 & -2 & 1 & 1 & 1 & 1 \\ 0 & 1 & 0 & -1 & 0 & 1 & -1 & -1 & 1 \\ 0 & -2 & 0 & 2 & 0 & 1 & -1 & -1 & 1 \\ 0 & 0 & 1 & 0 & -1 & 1 & 1 & -1 & 1 \\ 0 & 0 & -2 & 0 & 2 & 1 & 1 & -1 & -1 \\ 0 & 1 & -1 & 1 & -1 & 0 & 0 & 0 & 0 \\ 0 & 0 & 0 & 0 & 0 & 1 & -1 & 1 & -1 \end{bmatrix} \tag{5}$$

In Eq. 3, $\hat{\mathbf{S}}$ is the diagonal relaxation matrix in velocity moments. The kinetic viscosity is related to $\hat{\mathbf{S}}$ as:

$$s_i = \begin{cases} 1, & i = 0,3,5 \\ 1.4, & i = 1,2 \\ 1.2, & i = 4,6 \\ \frac{\delta_x^2}{\delta_t \nu + 0.5}, & i = 7,8 \end{cases}$$

Here the Mach number is defined as the ratio of the maximum velocity to C. When $Ma \ll 1$, the LBE can be used to recover the Navier-Stokes equation. More detail can be found in [36]. The macroscopic fluid properties such as density ρ and flow velocity $\overrightarrow{u}$ can be determined by the zero-th and the first order moment of the distribution function:

$$\begin{aligned} \rho(\overrightarrow{x}) &= \textstyle\sum_{i=0}^{14} f_i(\overrightarrow{x}), \\ \overrightarrow{u}(\overrightarrow{x}) &= \tfrac{1}{\rho(\overrightarrow{x})} \textstyle\sum_{i=0}^{14} f_i(\overrightarrow{x})\overrightarrow{e}_i, \end{aligned} \tag{6}$$

2.2. Discrete element method for the motion of particles

The motion of particles is simulated by using the DEM [38]. Newton's second law is applied to all particles in both the translational and rotational forms:

$$\begin{aligned} m_i \overrightarrow{a}_i &= m_i \overrightarrow{g} + \overrightarrow{F}_i^c + \overrightarrow{F}_i^h, \\ I_i \frac{d}{dt} \overrightarrow{\omega}_i &= \overrightarrow{T}_i^c + \overrightarrow{T}_i^h, \end{aligned} \tag{7}$$

where m_i and I_i are the mass and inertia of particle i, respectively. $\overrightarrow{a}_i$ is the acceleration. $\overrightarrow{\omega}_i$ is the angular velocity. Forces acting on particle i include gravitational force $m_i \overrightarrow{g}$, the hydrodynamic force $\overrightarrow{F}_i^h$ and the contact force $\overrightarrow{F}_i^c$. $\overrightarrow{T}_i^h$ and $\overrightarrow{T}_i^c$ represent torques due to the hydrodynamic and contact force. g is the gravitational constant.

Within the DE formalism, there are various kinds of contact laws used to determine the contact Force $\overrightarrow{F}_i^c$. In most of the DE-LBM studies, the linear normal contact model is used with the normal component of $\overrightarrow{F}_i^c$ given by:

$$F_i^{cn} = k_n \delta, \tag{8}$$

where δ is the particle overlapping distance and k_n is the particle contact spring stiffness. Another widely used contact law, mostly in the context of uncoupled DE, is the Hertz contact model [39] which takes into account the elastic deformation at the particle surface a

$$F_i^{cn} = k_n \delta^{\frac{3}{2}}, \tag{9}$$

All these previous contact models depend on the particle overlapping distance δ. Here, we develop a contact model based on the overlapping area A_c since both δ and A_c can be used to determine the magnitude of overlap.

$$F_i^{cn} = \alpha k_n A_c + \eta(\overrightarrow{v_j} - \overrightarrow{v_i}) \cdot \overrightarrow{n}, \tag{10}$$

where η is the damping coefficient, $\eta = 2\eta_0 \sqrt{\frac{k_n(m_i+m_j)}{m_i m_j}}$ with η_0 set to 0.34 in this study. $\overrightarrow{v_j}$ and $\overrightarrow{v_i}$ are translational velocity of contact particles i and j, respectively. The unit vector $\overrightarrow{n}$ points from j to i. An equivalent coefficient α is used to transfer A_c to δ. The second term on the right hand of Eq. 10 repesents the energy dissipation due to the frictional contact. The dissipative force linearly depends on the ralitive velocity. It should be pointed that η should increases with the ralitive velocity in aboved partly nonlinear

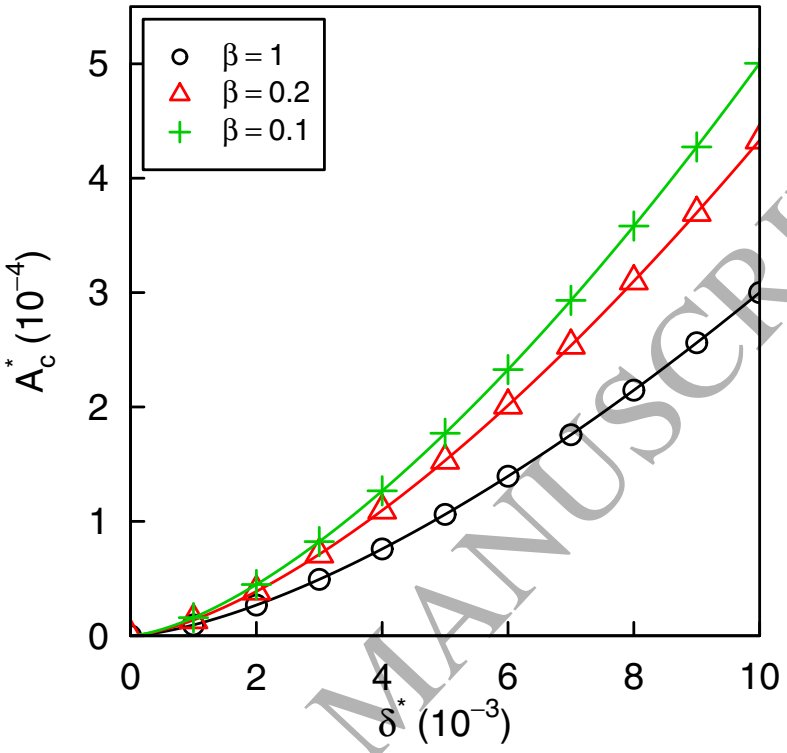

Figure 2: Dimensionless overlapping area as a function of dimensionless overlapping distance. Solid lines are regressions with the form of Eq. 11.

model [40, 41]. Kuwabara and Kono proposed a fully nonlinear model which can be found in [42]. As one can see, the normal contact force depends on A_c linearly. It can be proved that this model is equivalent to the Hertz contact model. Fig. 2 shows that the relationship between the overlapping area and the overlapping distance follows a power law:

$$A_c^* = f(\beta){\delta^*}^{\frac{3}{2}} \tag{11}$$

where the overlapping area and overlapping distance are normalized as $A_c^* = \frac{A_c(R_i^2+R_j^2)}{\pi R_i R_j}$ and $\delta^* = \frac{\delta(R_i+R_j)}{R_i R_j}$. β is the ratio of the particle radius: $\beta = \frac{R_j}{R_i}$ and here we assume $R_j \geq R_i$. With the substitution of Eq. 11, Eq. 10 can be reduced to Eq. 9 if $\alpha = f(\beta)$ and the damping force is neglected.

2.3. Coupling approach for LBM and DEM particles

To model the fluid-solid interaction, the hydrodynamic force $\overrightarrow{F}_i^h$ and torque $\overrightarrow{T}_i^h$ in Eq. 7 should be determined to solve the motion of particles. The non-slip boundary condition should be imposed on the surface of particles for the fluid. A modified LBM was introduced by Owen [43] in which the immersed boundary method [44] is adopted. The LBE is modified as follows:

$$f_i(\overrightarrow{x} + \overrightarrow{e}_i\delta t, t+\delta t) = f_i(\overrightarrow{x}, t) + B_n\Omega_i^s + (1-B_n)\left[\frac{\delta t}{\tau}(f_i^{eq} - f_i)\right], \quad (12)$$

where B_n is a weighting function depending on the occupation fraction ε_n. Ω_i^s is an additional collision term that accounts for the momentum exchange between fluid and moving particles. The bounce-back rule is applied to the interface of fluid and solid. The form of Ω_i^s proposed by Nobel [22] is given by:

$$\Omega_i^s = \left[f_{i'}(\overrightarrow{x}, t) - f_{i'}^{eq}(\rho, \overrightarrow{v}_p)\right] - \left[f_i(\overrightarrow{x}, t) - f_i^{eq}(\rho, \overrightarrow{v}_p)\right], \quad (13)$$

where the symbol i' denotes the direction opposite to the i direction, and $\overrightarrow{v}_p$ is the velocity of the particle at position x computed as:

$$\overrightarrow{v}_p = \overrightarrow{\omega} \times (\overrightarrow{x} - \overrightarrow{x}_c) + \overrightarrow{v}_c, \quad (14)$$

where $\overrightarrow{v}_c$ and $\overrightarrow{\omega}$ are the translational velocity and angular velocity at the particle's centroid, respectively.

The advantage of the above equation is that it transforms smoothly between fluid nodes and solid nodes due to the motion of particles. When $\varepsilon_n = 0$, Eq. 12 recovers the original LBE, while $\varepsilon_n = 1$ gives:

$$f_i(\overrightarrow{x} + \overrightarrow{e}_i\delta t, t+\delta t) = f_{i'}(\overrightarrow{x}, t) + \left[f_i^{eq}(\rho, \overrightarrow{v}_p) - f_{i'}^{eq}(\rho, \overrightarrow{v}_p)\right], \quad (15)$$

It should be noticed that Ladd [21] proposed a widely used moving solid-fluid boundary condition, which is defined as:

$$\begin{aligned} f_i(\overrightarrow{x} + \overrightarrow{e}_i\delta t, t+\delta t) &= f_{i'}^{+}(\overrightarrow{x}, t) + 6\omega_i\rho\frac{\overrightarrow{e}_i \cdot \overrightarrow{v}_p}{C^2} \\ &= f_{i'}^{+}(\overrightarrow{x}, t) + \left[f_i^{eq}(\rho, \overrightarrow{v}_p) - f_{i'}^{eq}(\rho, \overrightarrow{v}_p)\right], \end{aligned} \quad (16)$$

where $f_{i'}^{+}(\overrightarrow{x},t)$ is the distribution function after collision but before streaming.

Ladd's scheme can be considered as a special case ($\varepsilon_n = 1$) of the combination of Eq. 12 and Eq. 13. However, comparing Eq. 15 with Eq 16, one can find a difference concerning whether the distribution function values are taken after the collision step or not. Thus, without losing the advantage of Owen's scheme, a modified form of Eq. 12 and Eq. 13 is introduced here as:

$$f_i(\overrightarrow{x}+\overrightarrow{e}_i\delta t, t+\delta t) = f_i^{+}(\overrightarrow{x},t) + B_n\Omega_i^{s+}, \tag{17}$$

$$\Omega_i^{s+} = \left[f_{i'}^{+}(\overrightarrow{x},t) - f_{i'}^{eq}(\rho,\overrightarrow{v}_p)\right] - \left[f_i^{+}(\overrightarrow{x},t) - f_i^{eq}(\rho,\overrightarrow{v}_p)\right], \tag{18}$$

with symbol + denoting after collision and before streaming. It is clear that Eq. 17 and Eq. 18 can be combined to recover Eq. 16 when $\varepsilon_n = 1$.

Several forms of the weight function B_n have been discussed in [24] and [22]; however, the differences of these forms do not significantly affect the simulation results [24]. In this study, we apply B_n as given by [22]:

$$B_n(\varepsilon_n) = \frac{\varepsilon_n(s_7 - 1/2)}{(1-\varepsilon_n) + (s_7 - 1/2)}, \tag{19}$$

The total hydrodynamic force $\overrightarrow{F}_j^h$ and torque $\overrightarrow{T}_j^h$ over particle j covered by n cells can be calculated as:

$$\overrightarrow{F}_j^h = \frac{\delta_x^3}{\delta_t}\sum_n B_n\left(\sum_i \Omega_i^s\overrightarrow{e_i}\right), \tag{20}$$

$$\overrightarrow{T}_j^h = \frac{\delta_x^3}{\delta_t}\sum_n \left[(\overrightarrow{x} - \overrightarrow{x}_c)\times B_n\left(\sum_i \Omega_i^s\overrightarrow{e_i}\right)\right], \tag{21}$$

Fig.3 shows a problem which may occur when particles are too close to each other. If the lattice is covered by two particles, $\overrightarrow{v}_p$ and ϵ_n in Eq. 13 and 19 become non-unique. In such a case, we propose that the weighted average value is used to replace the original $\overrightarrow{v}_p$:

$$\overrightarrow{v}_p = \frac{\varepsilon_n(\overrightarrow{x},i)\overrightarrow{v}_p^i + \varepsilon_n(\overrightarrow{x},j)\overrightarrow{v}_p^j}{\varepsilon_n(\overrightarrow{x},i) + \varepsilon_n(\overrightarrow{x},j)}. \tag{22}$$

ε_n in Eq 19 also needs to be modified as $\varepsilon_n = \varepsilon_n(\overrightarrow{x},i) + \varepsilon_n(\overrightarrow{x},j)$ correspondingly.

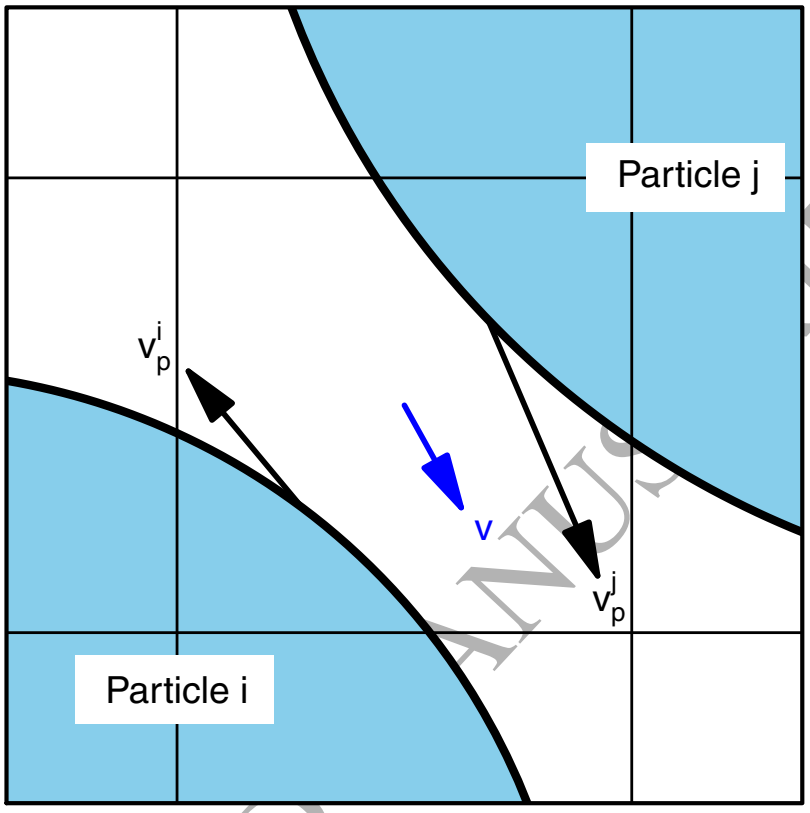

Figure 3: A lattice covered by two particles and $\varepsilon_n < 1$.

The occupation fraction (ε_n) plays an important role in the fluid-particles interaction. Several methods to calculate ε_n have been investigated in previous studies [20, 31, 43]: an exact closed-form solution, edges approximation, cell decomposition and polygonal approximation. To avoid the undesirable effects arising from the approximations, the exact closed-form solution is chosen in this study.

To update ε_n efficiently, a modified Verlet List method is [45] proposed based on the fact that the displacement of particles cannot be larger than one lattice size over each time step. Thus, only the ε_n values for boundary nodes and neighbouring nodes need to be updated as shown in Fig. 4. The boundary nodes are defined as $\overrightarrow{x_b} \in \{\overrightarrow{x} \mid \varepsilon_n(\overrightarrow{x}) \in (0,1)\}$ at the last time step and all lattices in the set $\{\overrightarrow{x_n} \mid \overrightarrow{x_n} = \overrightarrow{x_b} + \overrightarrow{e_i}, i = 1 \sim 8\}$ are neighbouring nodes.

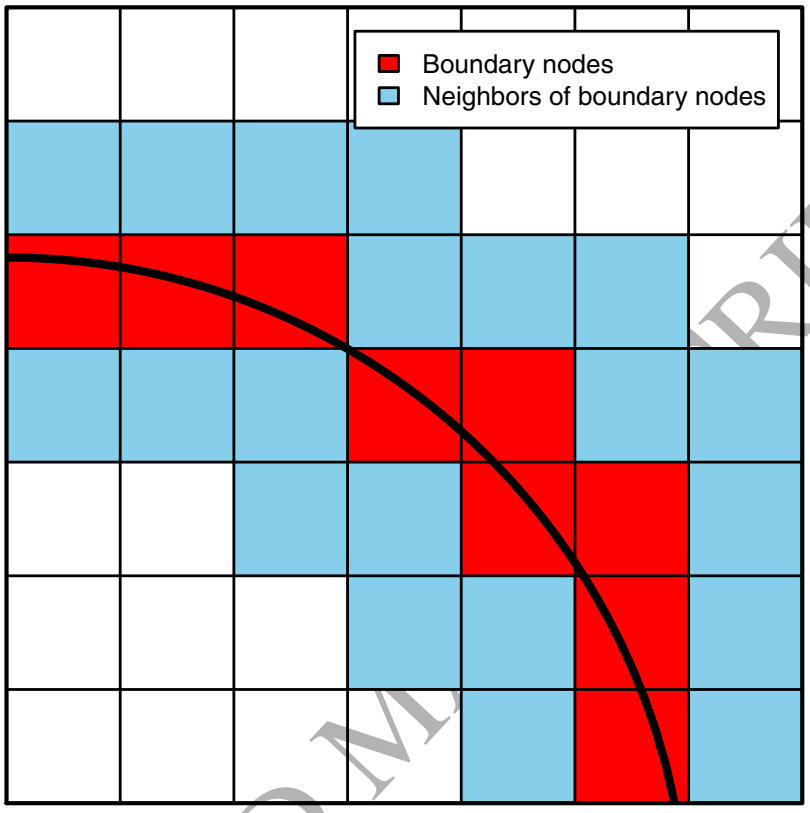

Figure 4: A modified Verlet List method.

2.4. An efficient contact detection algorithm for DE-LBM

The contact detection process takes a considerable proportion of the simulation time in DEM for a large number of particles moving freely in the system [46]. Several different contact detection algorithms have been proposed to speed up simulations [47]. Here we briefly introduce three most frequently mentioned algorithms: Verlet-Neighbor List [45], Linked Cell Method [48] and Linked Linear List [49]. In the Verlet-Neighbor method, each particle only checks the contact with its neighbouring particles at distances smaller than a cut-off radius. In contrast, the simulation domain is divided into lattices in the Linked Cell method, and the contact detection is only computed in the same square and the interface between squares. Finally, in the Linked Linear List method, a bounding box is defined around each particle and the contact between bounding boxes is determined. Once the contact between

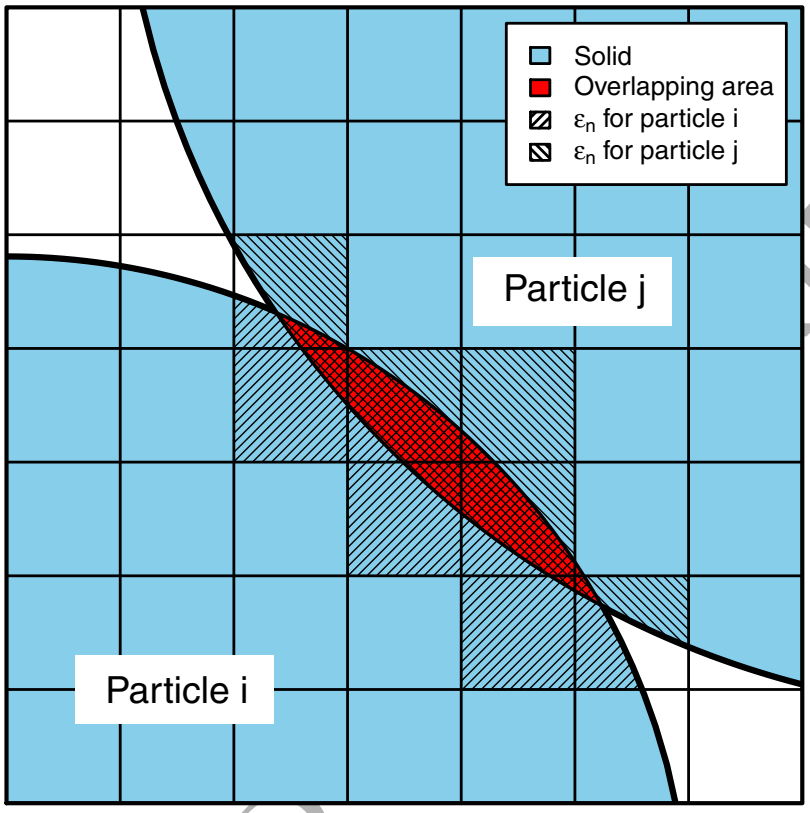

Figure 5: Overlapping area as a function of overlapping distance.

bounding boxes is found, the overlapping of two particles is evaluated. It can be shown that the computational cost of the Verlet-Neighbour List method and Linked Cell method present is of $O(N^2)$ whereas the cost of the Linked Linear List is of $O(N)$ (N is the total number of particles) [47].

So far, these methods are designed for DEM. However, within a coupled DE-LBM model, the existence of a lattice grid can be used to detect the contact with no additional calculations. As mentioned in 2.3, the occupation fraction (ε_n) has to be determined for solving the solid/fluid interaction. Here ε_n can also be used to detect the contact. Usually many cells will be involved for a particle pair, which is different from the condition assumed by the Linked Cell method where the lattice size is larger than the particle size. Thus, once a cell is covered by (two) different particles ($\varepsilon_n(\overrightarrow{x}, i) > 0$ and $\varepsilon_n(\overrightarrow{x}, j) > 0$, where $\overrightarrow{x}$ is the position of lattice, i and j are the

particles indexes), a contact is detected as shown in Fig. 5. Furthermore, the overlapping area A_c can be approximated as follows:

$$A_c = \sum_{k \in \Gamma} A_c^k(\overrightarrow{x_k}) \tag{23}$$

$$A_c^k(\overrightarrow{x_k}) = \begin{cases} \varepsilon_n(\overrightarrow{x_k}, i) + \varepsilon_n(\overrightarrow{x_k}, j) - A_m, & \text{if } \varepsilon_n(\overrightarrow{x_k}, i) + \varepsilon_n(\overrightarrow{x_k}, j) > A_m \\ 0, & \text{else} \end{cases} \tag{24}$$

where Γ is the set of cells satisfying $\{k \mid \varepsilon_n(\overrightarrow{x_k}, i) > 0, \varepsilon_n(\overrightarrow{x_k}, j) > 0\}$ and A_m is an approximation parameter (0.95 used in this study).

The execution times of Linked Cell method and present method are shown in Fig. 6. It is clear that the computational costs of present method do not depend on the number of particles. In contrast, the execution times of Linked Cell method increase significantly with the number of particles.

3. Validation

3.1. Validation for motions of single particle

To validate the new method presented above, the settling of a single particle in a viscous fluid is simulated to examine its dynamic behavior and associated fluid motion. The domain size is chosen as $100R \times 160R$ to minimize the effect of domain boundaries, with the particle radius R set to the 10 LBM-lattice size. The particle is placed at a height of $144R$ from the bottom of the domain. The initial transverse coordinate of the particle is slightly deviated from the centreline (by 2 LBM lattices) to induce unsteady motion at high Reynolds number. The density ratio of the particle and fluid is set as $\frac{\rho_s}{\rho_f} = 1.01$. The kinematic viscosity ν is varied as 0.05, 0.025, 0.02, 0.01 and 0.005 (in lattice units) to explore a wide range of Reynolds numbers. Wall boundary conditions are applied at the boundaries. Note that in the simulations, the gravity is only applied to the particle and thus a relative gravity given by $(1 - \rho_f/\rho_s)g$ is used as suggested by Feng [50].

Fig. 7 show the drag coefficient C_D of the single particle as a function of Reynolds number Re. For comparison, experiment results from Tritton [51] and Fornberg et al. [52] are also plotted. The Reynolds number and drag coefficient are defined as $Re = \frac{2v_pR}{\nu}$ and $C_D = \frac{8Rg(\rho_s - \rho_f)}{3\rho_f v_p^2}$, respectively. Overall, the simulation results agree well with the experimental data. When Re

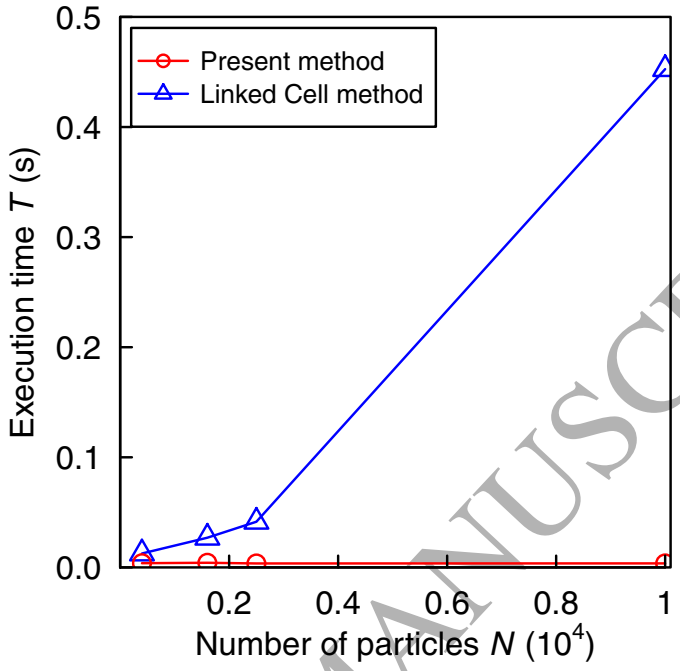

Figure 6: Comparison of the computational efficiency for Linked Cell method and present method. The domain size is 1000×1000 which is divided to cells with size of 200×200. The number of time steps is 100.

is larger than 100, our model predicts slightly higher values than the ones from Fornberg's experiments since the particle is in a state of free settling in fluid during the simulations in contrast to the controlled motion of a fixed cylinder used in the experiments. The vorticity fields around the particle for $\nu = 0.05, 0.01$ are shown at Fig. 8. The size of vortices behind the particle increase with Re. The structure of these vortices play an important role in particle-fluid interactions [30].

Simulations of a rotating particle immersed in a uniform flow are also carried out to further validate this model. Boundary conditions are set as the velocity inlet on the left side and zero velocity gradient outlet for the right side. The top and bottom boundaries are set as solid walls. The particle is set to spin with a constant angular velocity ω. An additional lift force acts on the particle due to the rotation. This phenomenon is due to the well-known Magnus effect. A lift coefficient, which indicates the magnitude of the lift

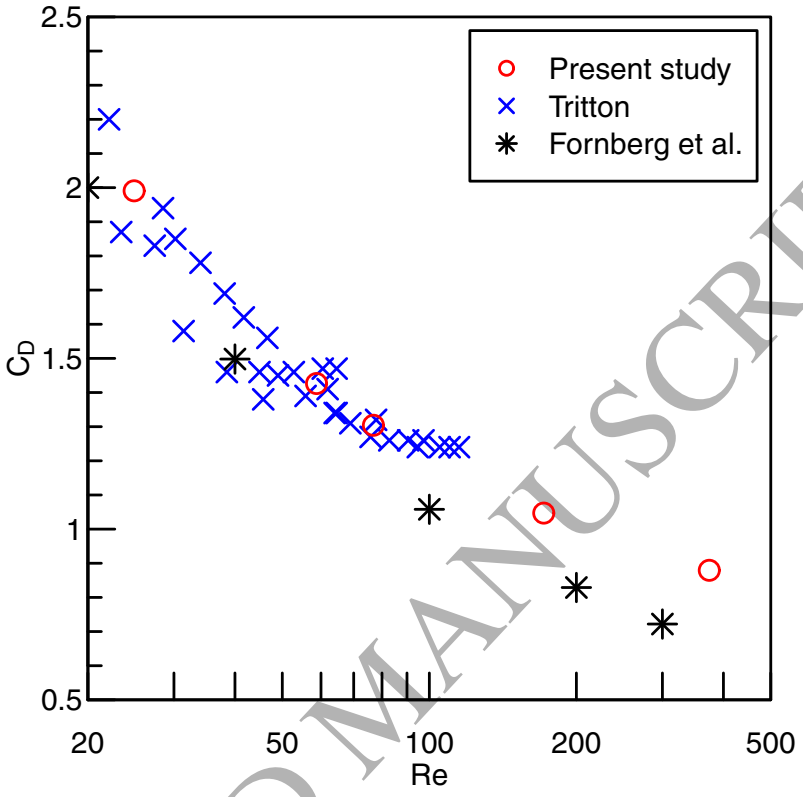

Figure 7: Drag coefficient C_D of a single particle as a function of Re.

force, can be obtained as $C_L = \frac{F_y}{\rho_f U^2 R}$ depending on the lift force F_y. Here, the Reynolds number is defined as $Re = \frac{2UR}{\nu}$, where U is the unperturbed mainstream speed (along the x-direction). Another dimensionless number is the spin number $S_{pa} = \frac{\omega R}{U}$. Fig. 9 shows the lift coefficient varying with the spin number linearly at $Re = 20$. It also shows an excellent agreement with the results of Kang et al. [53] and Ingham and Tang [54].

3.2. Validation for the settling of two in-line particle with the contact model

In order to validate the contact model presented in 2.2, we conduct a simulation of the settling of two particles. The same particle radius R and density ratio $\frac{\rho_s}{\rho_f}$ are used as in 3.1. The domain size is $20R \times 80R$ and the kinetic viscosity $\nu = 0.05$. Two particles are placed at $72R$ and $68R$ from the bottom initially, and the higher particle is placed 0.1 LBM lattice size off

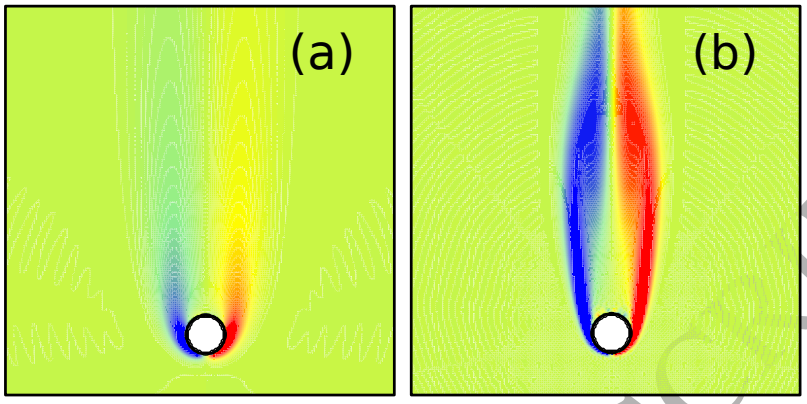

Figure 8: Vorticity fields for (a) $\nu = 0.05$, and (b) $\nu = 0.01$.

the centreline. The stiffness is set to $k_n = 0.25$ and the equivalent coefficient $\alpha = 0.3$.

These two particles are driven by gravity and undergo a motion often referred to as "drafting, kissing and tumbling" (DKT), which was first numerically studied by Feng et al. [50]. Fig. 10 and Fig. 11 show time series of vertical coordinate of particle centre and particle vertical velocity in comparison with the results of [50]. It can be seen that the DKT motions are successfully simulated with the presented method, indicating that the present overlapping area contact model gives similar results to those of the overlapping distances contact model. The minor differences between the present model predictions and Feng's results may be due to the different ways of solving particle-fluid interactions and hence a slightly different hydraulic forces in both studies (as evident in Fig. 11 where differences between the velocities calculated from both methods can be seen before the particles come in contact with each other).

4. Application examples

4.1. The settling of a large number of particles

In this section, the settling of a large number (2500) of particles in a closed box is simulated. Particles have a size of $R = 5$ cells to reduce the computational cost. A larger domain ($200R \times 200R$) is chosen and the parameters are the same as in the last section. Random initial positions for the particles are set as follows: the domain is divided into squares of $L = 4R$

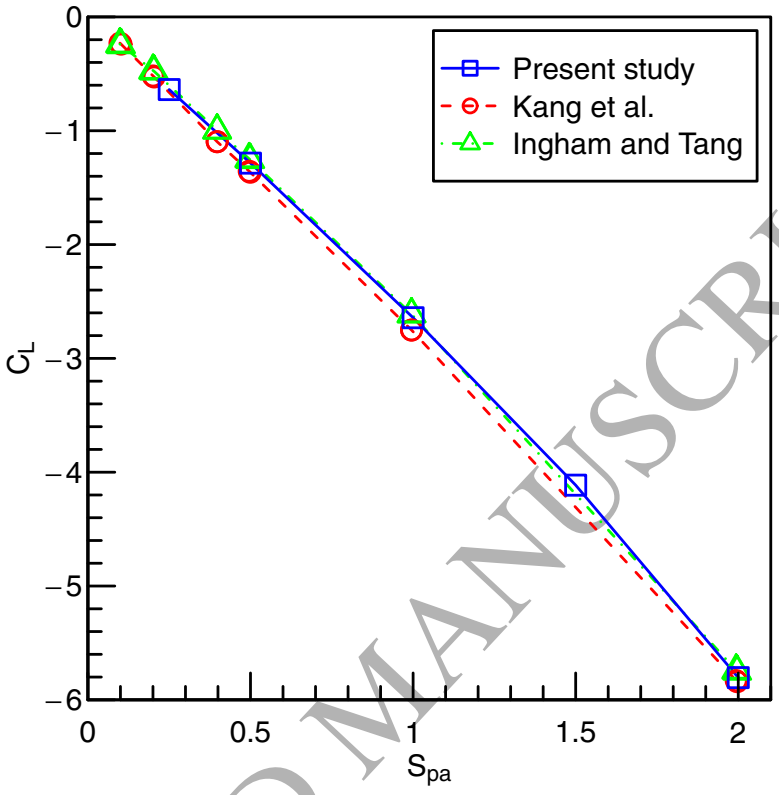

Figure 9: Lift coefficient C_L as a function of the spin number S_{pa}.

and every square only contains one particle with a random inside position as shown in Fig. 12(a). This gives a solid volume (area) fraction $\phi_0 = 0.196$. Fig. 12 shows snapshots of the velocity field at different times of the simulation. After a short free settling stage, the particles tend to move in clusters due to the collision and KDT motions. Complex fluid structures can be found at different scales, with several paths being created by leading and following particles preferring to move along those trails of reduced drag. Fig. 13 shows that the settling interface position depends on the time linearly, indicting a relatively constant settling speed. The interface position is determined by the average height of the highest particles cross the domain. The vertical concentration ϕ profiles is presented in Fig. 14. To calculate this profile, the domain is divided into several layers in the vertical direction and the concentration of each layer is calculated as the solid volume (area) fraction in

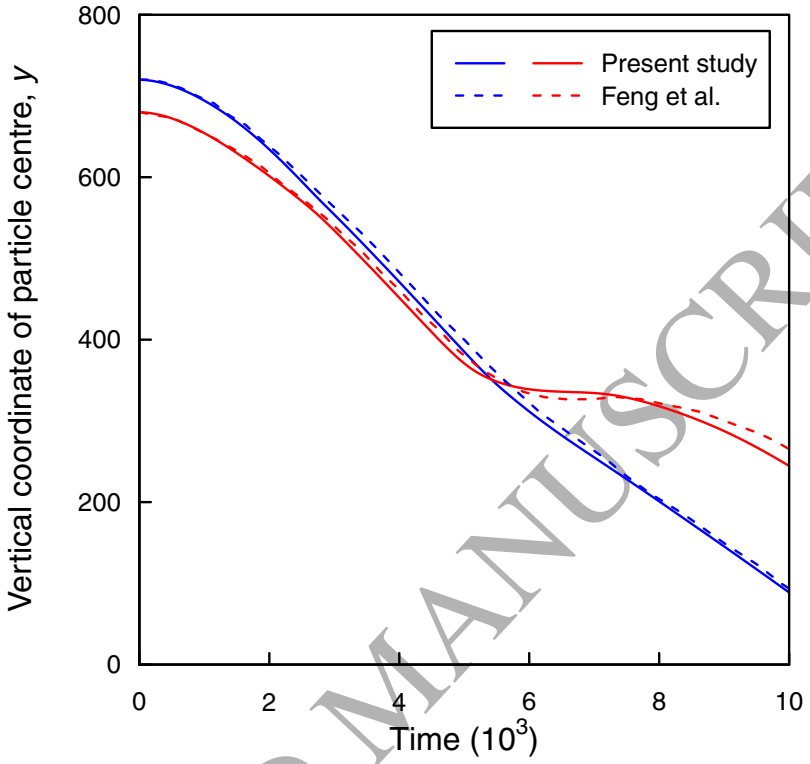

Figure 10: Time series of vertical coordinate of particle centre. Red and blue color represent the leading particle and the following particle, respectively.

the layer. Two sudden jumps of concentration are found between the different layers. From the top to the bottom, the concentration increases sharply from 0 to ϕ_0 and the value of ϕ is mostly kept constant until particles approach the bottom. Then ϕ linearly increases to the maximum concentration $\pi_{max} = 0.785$. Bürger and Tory [55] reported seven different settling modes for homogeneous suspensions based on the analytical analysis of Kynch's theory [56]. Our results show qualitatively an agreement with the 'MS-3' mode (the embedded figure of Fig. 14). An interesting difference between the simulation and analytical results is: the concentration in the dense layer is a constant for the 'MS-3' mode; however our simulation shows a linear dependence of the concentration with the height. In Fig. 12, different colors of particles are used to indicate their initial positions. The final positions of

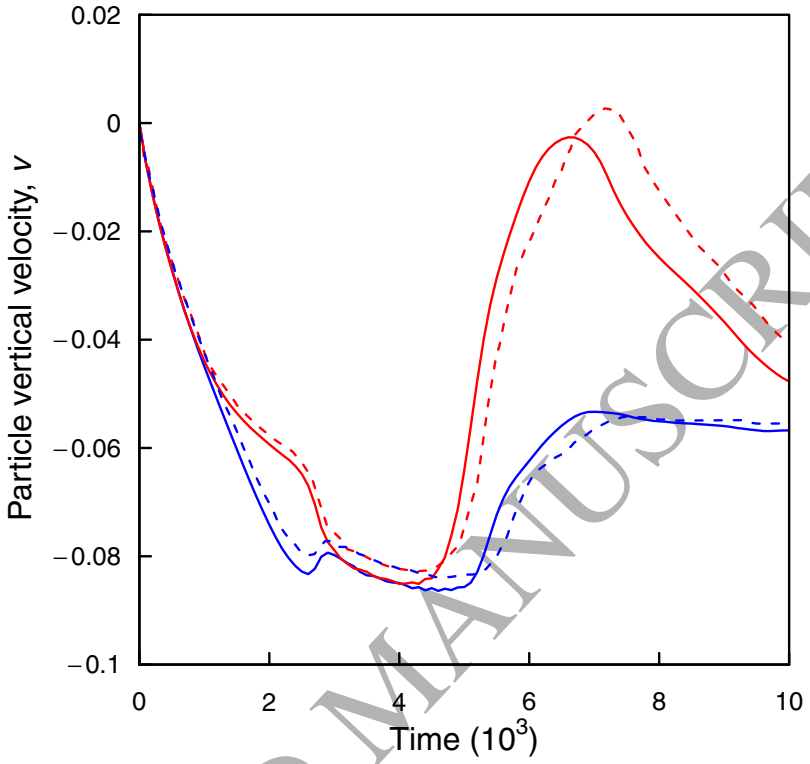

Figure 11: Time series of particle's vertical velocity.

particles do not follow the order of the initial conditions, indicating strong mixing of particles from different layers during the settling. To study the mixing process, we define a mixing index as

$$\Lambda_l = \frac{\sum_{i \in \Gamma_l} \zeta_i^{init}}{N_{pl}} \tag{25}$$

where Γ_l is the set of all particles belonging to the lth layer (same layers as used for calculating the vertical concentration profile) and N_{pl} is the number of particles in Γ_l. ζ_i^{init} is a dimensionless number given by $\frac{l_0}{N_l}$, where N_l is the total number of layers and l_0 indicate the initial layer of particle i at the beginning of the simulation. Fig. 15 shows the profiles of Λ at different times. A clear stratification is found during the sedimentation: Λ linearly increases with the height from the bottom; however, above the dense layer,

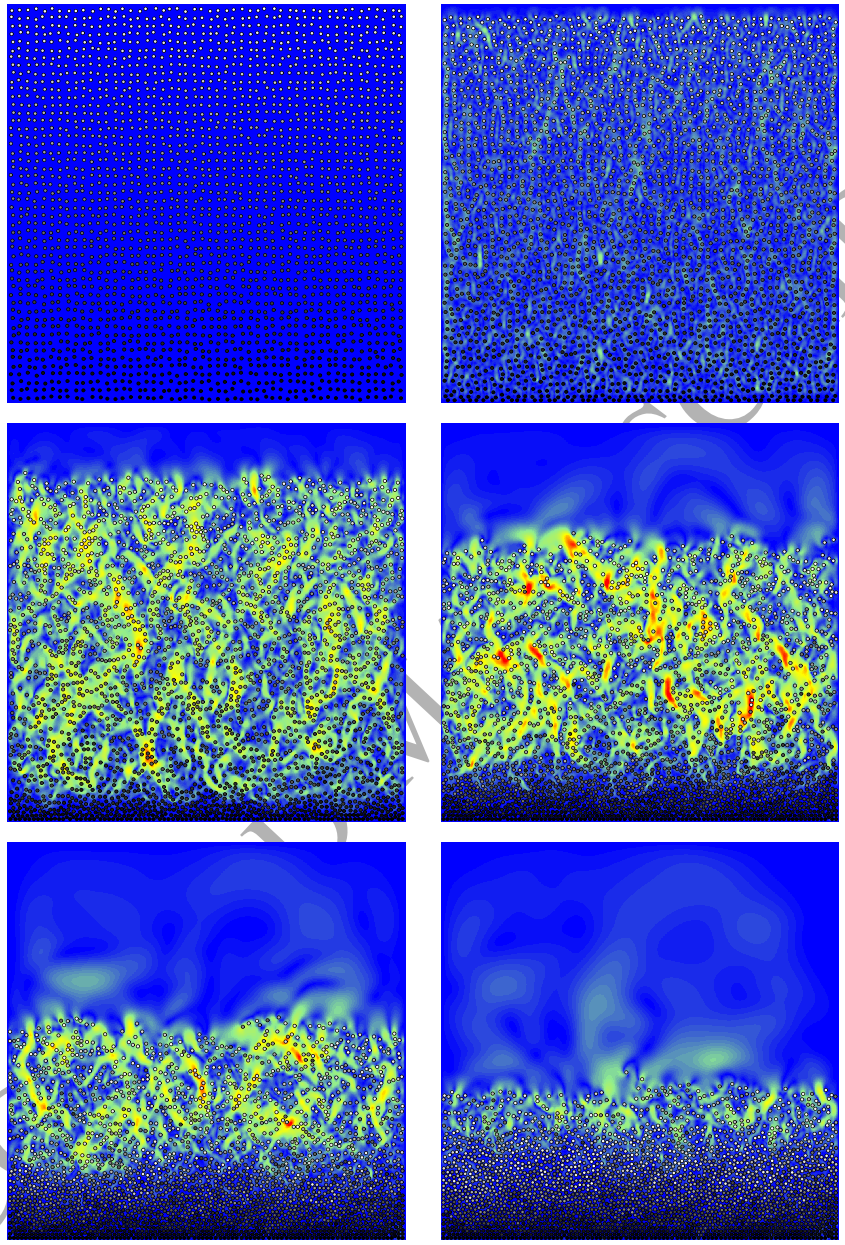

Figure 12: Snapshots of 2500 particles settling at different times. The color of particles indicates the initial position. The colourmap is proportional to the fluid velocity.

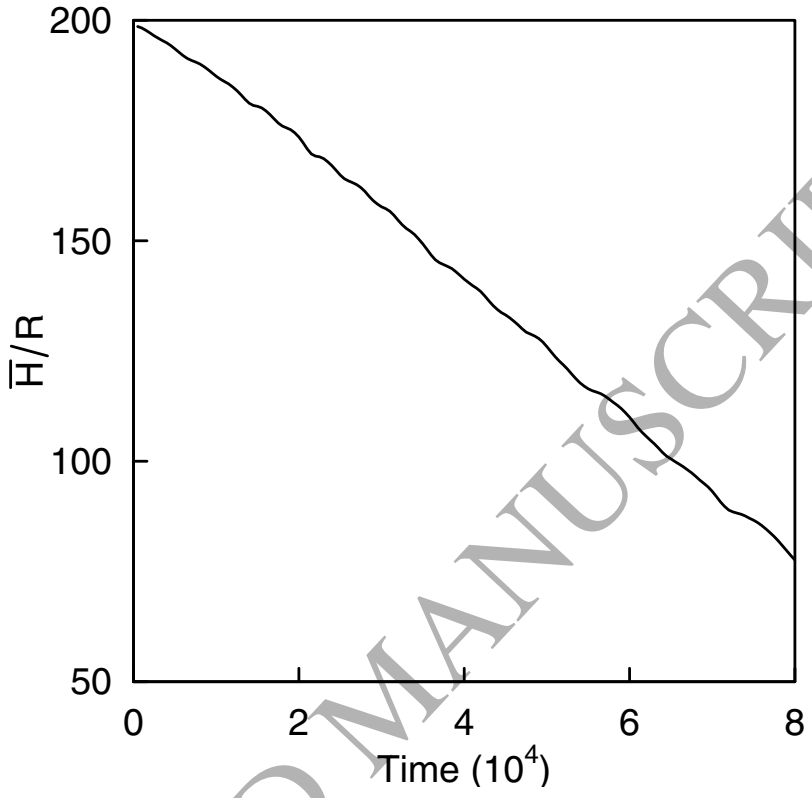

Figure 13: Time evolution of the interface position.

Λ is not as sensitive to the height. It may be concluded that all particles in this section are well mixed due to the observed flow patterns. The mixing appears to have occurred over a much larger scale compared to the particle size.

5. Concluding remarks

An efficient DE-LBM scheme has been developed in this study. We introduce a novel contact detection algorithm based on the occupation fraction (ε_n) for both the particle-fluid and particle-particle interaction, which requires no additional calculations. This method can reduce the DE-LBM simulation time significantly. Instead of using the overlapping distance, the contact model is modified to be based on the particle overlapping area (calculated from ε_n). The modified contact model is shown to be equivalent

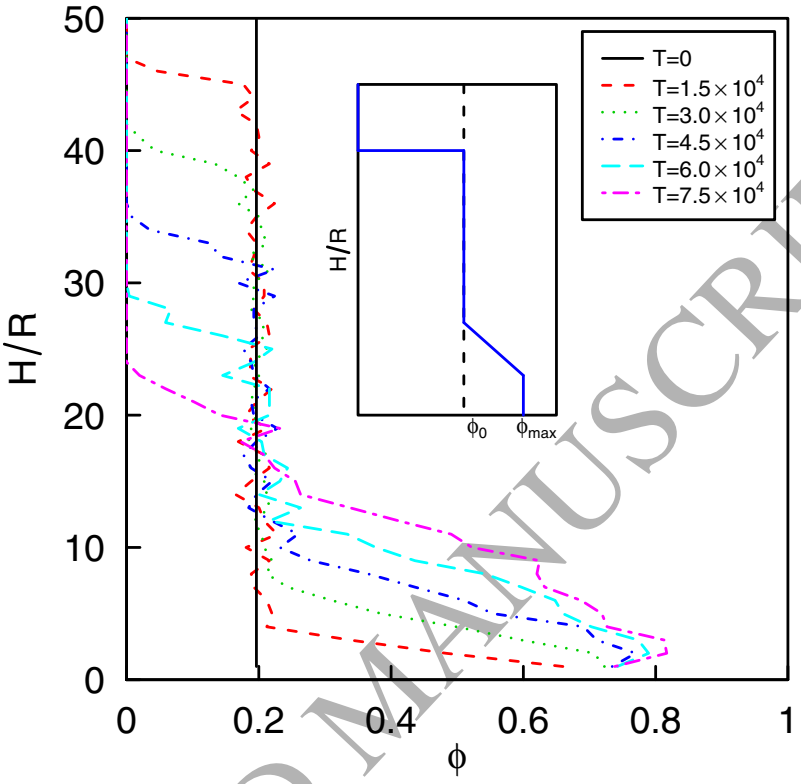

Figure 14: Vertical concentration profiles at different times.

to the classical Hertz contact model. The multiple relaxation time (MRT) collision operator is employed to increase the numerical stability of LBM. The coupling approach is also constructed to unify the different treatments made in Ladd's and Owen's schemes. To further speed up the simulation, a modified Verlet List method is introduced.

The model was first validated for the settling of a circular particle immersed in fluid. The simulated drag coefficient shows a good agreement with experimental results of Tritton [51] and Fornberg et al. [52] for flows passing a fixed cylinder. The lift coefficients acting on a rotating cylinder are also simulated well and agree with previous studies [53, 54]. Moreover, the present model successfully simulates the DKT motions. The proposed overlapping area contact model gives similar results to those predicted by the overlapping distance contact model.

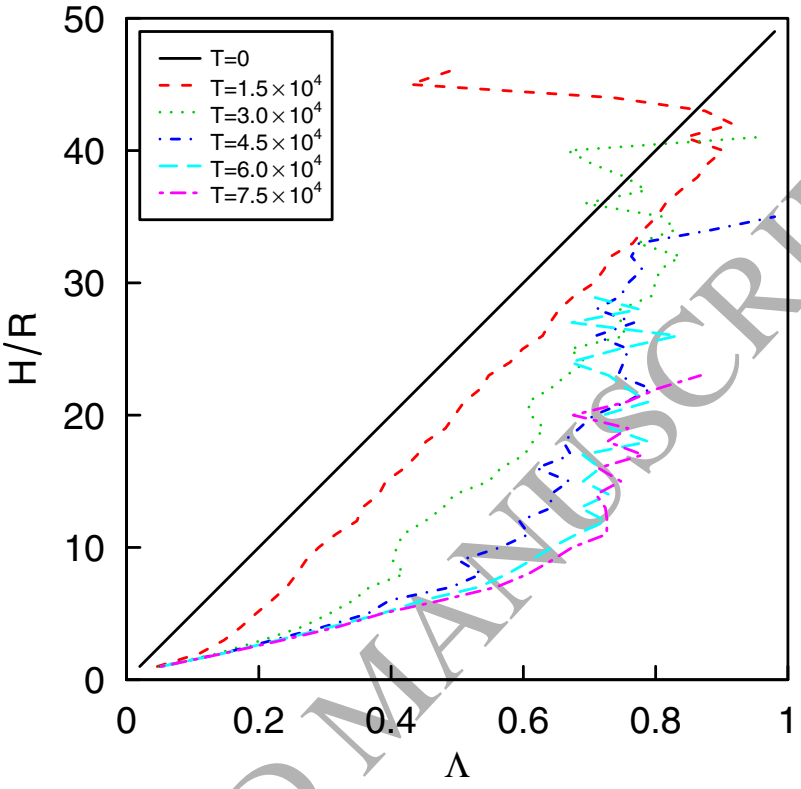

Figure 15: Time series of particle mixing index.

The present DE-LBM model is applied to simulate the settling of a large number (2500) of particles. With a large number of particles far smaller than the ones commonly found in settling experiments, the concentration profiles given by the DE-LBM simulation match well with the analytical solution. Details provided by the simulation allow us to quantitatively study the particle-mixing process during settling. A clear stratification is found for the mixing index, providing details on the different phases involved in the mixing process.

The presented results demonstrate the potential of the new DE-LBM model as a powerful numerical tool for simulating a wide range of particulate systems that can be found in many engineering and science disciplines. Future studies will focus on extending this method to 3D as well as for general shaped particles.

Acknowledgement

We gratefully acknowledge the funding support from the Natural Science Foundation of China (51239003, 51679065), the ARC Discovery project (DP140100490, LP150101110). The first author would like to thanks Professor E.M. Tory for helpful discussions. The second author would like to acknowledge the support from the Advance Queensland Fellowship program (Grant number AQ-15188).

References

[1] S. Tran-Cong, M. Gay, E. E. Michaelides, Drag coefficients of irregularly shaped particles, Powder Technology 139 (2004) 21–32.

[2] A. Haider, O. Levenspiel, Drag coefficient and terminal velocity of spherical and nonspherical particles, Powder technology 58 (1989) 63–70.

[3] R. Clift, J. R. Grace, M. E. Weber, Bubbles, drops, and particles, Courier Corporation, 2005.

[4] A. Khan, J. Richardson, The resistance to motion of a solid sphere in a fluid, Chemical Engineering Communications 62 (1987) 135–150.

[5] F. M. White, Fluid mechanics, 2003.

[6] D. Leith, Drag on nonspherical objects, Aerosol science and technology 6 (1987) 153–161.

[7] G. H. Ganser, A rational approach to drag prediction of spherical and nonspherical particles, Powder Technology 77 (1993) 143–152.

[8] E. Loth, Drag of non-spherical solid particles of regular and irregular shape, Powder Technology 182 (2008) 342–353.

[9] N. Clark, P. Gabriele, S. Shuker, R. Turton, Drag coefficient of irregular particles in newton's settling regime, Powder technology 59 (1989) 69–72.

[10] E. Pettyjohn, E. Christiansen, Effect of particle shape on free-settling rates of isometric particles, Chemical Engineering Progress 44 (1948) 157–172.

[11] N.-S. Cheng, Simplified settling velocity formula for sediment particle, Journal of hydraulic engineering 123 (1997) 149–152.

[12] A. Ten Cate, C. Nieuwstad, J. Derksen, H. Van den Akker, Particle imaging velocimetry experiments and lattice-boltzmann simulations on a single sphere settling under gravity, Physics of Fluids (1994-present) 14 (2002) 4012–4025.

[13] S. B. Field, M. Klaus, M. Moore, F. Nori, Chaotic dynamics of falling disks, Nature 388 (1997) 252–254.

[14] W. W. Willmarth, N. E. Hawk, R. L. Harvey, Steady and unsteady motions and wakes of freely falling disks (1964).

[15] E. Marchildon, A. Clamen, W. Gauvin, Drag and oscillatory motion of freely falling cylindrical particles, The Canadian Journal of Chemical Engineering 42 (1964) 178–182.

[16] S.-j. Guo, F.-h. Zhang, X.-g. Song, B.-t. Wang, Deposited sediment settlement and consolidation mechanisms, Water Science and Engineering 8 (2015) 335–344.

[17] P. A. Cundall, O. D. Strack, A discrete numerical model for granular assemblies, Geotechnique 29 (1979) 47–65.

[18] N. Belheine, J.-P. Plassiard, F.-V. Donzé, F. Darve, A. Seridi, Numerical simulation of drained triaxial test using 3d discrete element modeling, Computers and Geotechnics 36 (2009) 320–331.

[19] J. Cabrejos-Hurtado, S. Galindo Torres, D. Pedroso, Assessment of the mechanical behaviour of granular media by dem-based true triaxial tests, in: Applied Mechanics and Materials, volume 846, Trans Tech Publ, pp. 428–433.

[20] S. Galindo-Torres, A coupled discrete element lattice boltzmann method for the simulation of fluid–solid interaction with particles of general shapes, Computer Methods in Applied Mechanics and Engineering 265 (2013) 107–119.

[21] A. J. Ladd, Numerical simulations of particulate suspensions via a discretized boltzmann equation. part 1. theoretical foundation, Journal of Fluid Mechanics 271 (1994) 285–309.

[22] D. Noble, J. Torczynski, A lattice-boltzmann method for partially saturated computational cells, International Journal of Modern Physics C 9 (1998) 1189–1201.

[23] B. K. Cook, D. R. Noble, J. R. Williams, A direct simulation method for particle-fluid systems, Engineering Computations 21 (2004) 151–168.

[24] Y. Feng, K. Han, D. Owen, Coupled lattice boltzmann method and discrete element modelling of particle transport in turbulent fluid flows: Computational issues, International Journal for Numerical Methods in Engineering 72 (2007) 1111.

[25] S. Galindo-Torres, A. Scheuermann, H. Mühlhaus, D. Williams, A micro-mechanical approach for the study of contact erosion, Acta Geotechnica 10 (2015) 357–368.

[26] S. Galindo-Torres, D. Pedroso, D. Williams, L. Li, Breaking processes in three-dimensional bonded granular materials with general shapes, Computer Physics Communications 183 (2012) 266–277.

[27] S. Galindo-Torres, F. Alonso-Marroquín, Y. Wang, D. Pedroso, J. M. Castano, Molecular dynamics simulation of complex particles in three dimensions and the study of friction due to nonconvexity, Physical Review E 79 (2009) 060301.

[28] S. Galindo-Torres, D. Pedroso, Molecular dynamics simulations of complex-shaped particles using voronoi-based spheropolyhedra, Physical Review E 81 (2010) 061303.

[29] S. Galindo-Torres, D. Pedroso, D. Williams, H. Mühlhaus, Strength of non-spherical particles with anisotropic geometries under triaxial and shearing loading configurations, Granular Matter 15 (2013) 531–542.

[30] P. Zhang, S. Galindo-Torres, H. Tang, G. Jin, A. Scheuermann, L. Li, Lattice boltzmann simulations of settling behaviors of irregularly shaped particles, Physical Review E 93 (2016) 062612.

[31] L. Wang, G. Zhou, X. Wang, Q. Xiong, W. Ge, Direct numerical simulation of particle–fluid systems by combining time-driven hard-sphere model and lattice boltzmann method, Particuology 8 (2010) 379–382.

[32] L. Wang, B. Zhang, X. Wang, W. Ge, J. Li, Lattice boltzmann based discrete simulation for gas–solid fluidization, Chemical Engineering Science 101 (2013) 228–239.

[33] X. Cui, J. Li, A. Chan, D. Chapman, A 2d dem–lbm study on soil behaviour due to locally injected fluid, Particuology 10 (2012) 242–252.

[34] S. Galindo-Torres, A. Scheuermann, L. Li, Numerical study on the permeability in a tensorial form for laminar flow in anisotropic porous media, Physical Review E 86 (2012) 046306.

[35] S. Galindo-Torres, A. Scheuermann, L. Li, D. Pedroso, D. Williams, A lattice boltzmann model for studying transient effects during imbibition–drainage cycles in unsaturated soils, Computer Physics Communications 184 (2013) 1086–1093.

[36] A. A. Mohamad, Lattice Boltzmann method: fundamentals and engineering applications with computer codes, Springer Science & Business Media, 2011.

[37] P. Lallemand, L.-S. Luo, Theory of the lattice boltzmann method: Dispersion, dissipation, isotropy, galilean invariance, and stability, Physical Review E 61 (2000) 6546.

[38] S. Luding, Introduction to discrete element methods: basic of contact force models and how to perform the micro-macro transition to continuum theory, European Journal of Environmental and Civil Engineering 12 (2008) 785–826.

[39] B. Smeets, T. Odenthal, S. Vanmaercke, H. Ramon, Polygon-based contact description for modeling arbitrary polyhedra in the discrete element method, Computer Methods in Applied Mechanics and Engineering 290 (2015) 277–289.

[40] H. Kruggel-Emden, E. Simsek, S. Rickelt, S. Wirtz, V. Scherer, Review and extension of normal force models for the discrete element method, Powder Technology 171 (2007) 157–173.

[41] J. Lee, H. J. Herrmann, Angle of repose and angle of marginal stability: molecular dynamics of granular particles, Journal of Physics A: Mathematical and General 26 (1993) 373.

[42] G. Kuwabara, K. Kono, Restitution coefficient in a collision between two spheres, Japanese journal of applied physics 26 (1987) 1230.

[43] D. Owen, C. Leonardi, Y. Feng, An efficient framework for fluid–structure interaction using the lattice boltzmann method and immersed moving boundaries, International Journal for Numerical Methods in Engineering 87 (2011) 66–95.

[44] R. Mittal, G. Iaccarino, Immersed boundary methods, Annu. Rev. Fluid Mech. 37 (2005) 239–261.

[45] Z. Yao, J.-S. Wang, G.-R. Liu, M. Cheng, Improved neighbor list algorithm in molecular simulations using cell decomposition and data sorting method, Computer physics communications 161 (2004) 27–35.

[46] A. Munjiza, K. Andrews, Nbs contact detection algorithm for bodies of similar size, International Journal for Numerical Methods in Engineering 43 (1998) 131–149.

[47] B. Muth, M.-K. Müller, P. Eberhard, S. Luding, Collision detection and administration methods for many particles with different sizes, 4th International Conference on Discrete Element Methods, Brisbane, Australia (2007) 1–18.

[48] M. P. Allen, D. J. Tildesley, Computer simulation of liquids, Oxford university press, 1989.

[49] A. Schinner, Fast algorithms for the simulation of polygonal particles, Granular Matter 2 (1999) 35–43.

[50] Z.-G. Feng, E. E. Michaelides, The immersed boundary-lattice boltzmann method for solving fluid–particles interaction problems, Journal of Computational Physics 195 (2004) 602–628.

[51] D. Tritton, Experiments on the flow past a circular cylinder at low reynolds numbers, Journal of Fluid Mechanics 6 (1959) 547–567.

[52] B. Fornberg, A numerical study of steady viscous flow past a circular cylinder, Journal of Fluid Mechanics 98 (1980) 819–855.

[53] S. Kang, H. Choi, S. Lee, Laminar flow past a rotating circular cylinder, Physics of Fluids (1994-present) 11 (1999) 3312–3321.

[54] D. Ingham, T. Tang, A numerical investigation into the steady flow past a rotating circular cylinder at low and intermediate reynolds numbers, Journal of Computational Physics 87 (1990) 91–107.

[55] R. Bürger, E. M. Tory, On upper rarefaction waves in batch settling, Powder technology 108 (2000) 74–87.

[56] G. J. Kynch, A theory of sedimentation, Transactions of the Faraday society 48 (1952) 166–176.